OPEN ACCESS

Eigenanalysis of a neural network for optic flow processing

New Journal of Physics
The open-access journal for physics

Eigenanalysis of a neural network for optic flow processing

F Weber[1,3], H Eichner[1], H Cuntz[2] and A Borst[1]

[1] Department of Systems and Computational Neuroscience, Max-Planck-Institute of Neurobiology, Martinsried, Germany
[2] Wolfson Institute for Biomedical Research, Department of Physiology, University College London, UK
E-mail: weberf@neuro.mpg.de

New Journal of Physics **10** (2008) 015013 (21pp)
Received 15 June 2007
Published 31 January 2008
Online at http://www.njp.org/
doi:10.1088/1367-2630/10/1/015013

Abstract. Flies gain information about self-motion during free flight by processing images of the environment moving across their retina. The visual course control center in the brain of the blowfly contains, among others, a population of ten neurons, the so-called vertical system (VS) cells that are mainly sensitive to downward motion. VS cells are assumed to encode information about rotational optic flow induced by self-motion (Krapp and Hengstenberg 1996 *Nature* **384** 463–6). Recent evidence supports a connectivity scheme between the VS cells where neurons with neighboring receptive fields are connected to each other by electrical synapses at the axonal terminals, whereas the boundary neurons in the network are reciprocally coupled via inhibitory synapses (Haag and Borst 2004 *Nat. Neurosci.* **7** 628–34; Farrow *et al* 2005 *J. Neurosci.* **25** 3985–93; Cuntz *et al* 2007 *Proc. Natl Acad. Sci. USA*). Here, we investigate the functional properties of the VS network and its connectivity scheme by reducing a biophysically realistic network to a simplified model, where each cell is represented by a dendritic and axonal compartment only. Eigenanalysis of this model reveals that the whole population of VS cells projects the synaptic input provided from local motion detectors on to its behaviorally relevant components. The two major eigenvectors consist of a horizontal and a slanted line representing the distribution of vertical motion components across the fly's azimuth. They are, thus, ideally suited for reliably encoding translational

[3] Author to whom any correspondence should be addressed.

and rotational whole-field optic flow induced by respective flight maneuvers. The dimensionality reduction compensates for the contrast and texture dependence of the local motion detectors of the correlation-type, which becomes particularly pronounced when confronted with natural images and their highly inhomogeneous contrast distribution.

Contents

1. Introduction

1.1. General

Animals moving freely in three dimensions (3D) induce by their self-motion a permanent shift of the images on their retina. The resulting distribution of vectors across the retina is called optic flow. Flies heavily rely on optic flow to maintain a stable course through the surrounding environment [1, 2].

In the blowfly *Calliphora vicina*, optic flow information is encoded by a set of about 60 large-field motion-sensitive neurons. These so-called tangential cells are located in the lobula plate of each brain hemisphere. With their large dendrites they integrate output signals provided by retinotopically arranged local motion detectors [3, 4] and are connected to descending neurons controlling motor neurons for locomotion or head movements [5]. Each of the tangential cells can be uniquely identified because of its anatomical invariance and characteristic response properties to visual stimuli [6]–[8]. Among the tangential cells, a subgroup of three neurons, the so-called horizontal system (HS) cells [7], most strongly reacts to horizontal motion, whereas the 10 vertical system (VS) cells [7] preferentially respond to vertical downward motion. HS and VS cells encode information about visual motion stimuli mainly by graded shifts of their membrane potential [9] and are thought to constitute the principal output elements of the lobula plate. They respond to motion in their preferred direction with a positive membrane potential deflection (depolarization), whereas a motion in the opposite (null) direction induces a negative potential shift (hyperpolarization).

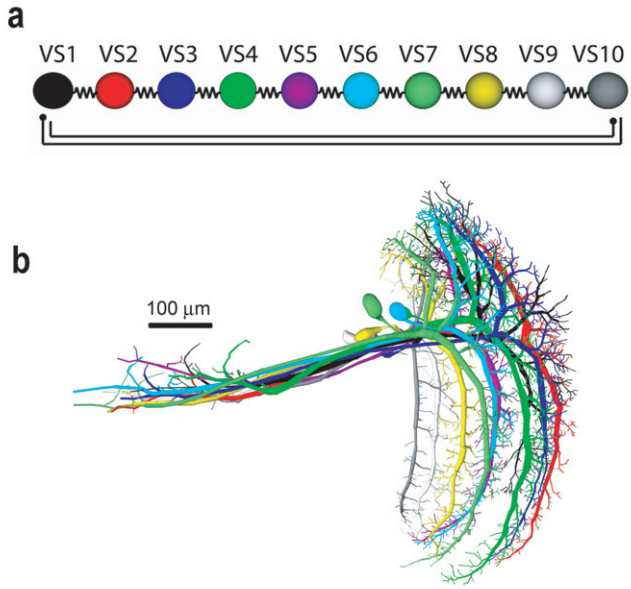

Figure 1. (a) Schematic sketch of the putative VS network: each VS cell is connected to its neighbors via electrical synapses. VS1 and VS10 are assumed to mutually inhibit each other. (b) Compartmental models of the 10 VS cells as obtained from 2-photon image stacks. Cells are arranged according to their position in the lobula plate. Reprinted with permission from [10].

1.2. The VS network

The dendrites of the VS cells are sequentially positioned within the lobula plate (and accordingly numbered) [7], where VS1 has the most lateral and VS10 the most medial dendrite. Figure 1(b) shows compartmental models of the 10 VS cells as reconstructed from two-photon image stacks [10] and arranged according to their location in the lobula plate.

The connectivity of the VS cells has been elucidated by intracellular dual-recordings [11]. The results of these experiments are consistent with a connectivity as depicted in figure 1(a) [10]–[12]: each VS cell is electrically coupled to its neighbors. VS1 and VS10 are mutually coupled via inhibitory chemical synapses. The location of electrical synapses has been revealed by measuring the Ca^{2+} concentration in neighboring VS cells when injecting currents into only one of them [10]. Previous experiments have shown that the Ca^{2+} concentration of VS cells depends linearly on the membrane potential [13]. The Ca^{2+} signal was strongest at the axonal terminal of the cell without current injection suggesting that the synapse connecting both cells is located in this region [10].

Corresponding to the retinotopic organization of the lobula plate, the receptive fields of the VS cells of one brain hemisphere are also sequentially arranged, thus nearly covering one half of the visual surround of the fly. VS1 has a frontal, whereas VS10 exhibits a caudal receptive field [14]. Figure 2 shows that the azimuth of the peak sensitivity to vertical downward and upward motion shifts from a frontal to a caudal position for VS1–VS9 [15]. VS10 has been omitted from experimental analysis because of the location of its receptive field, which made it impossible to stimulate.

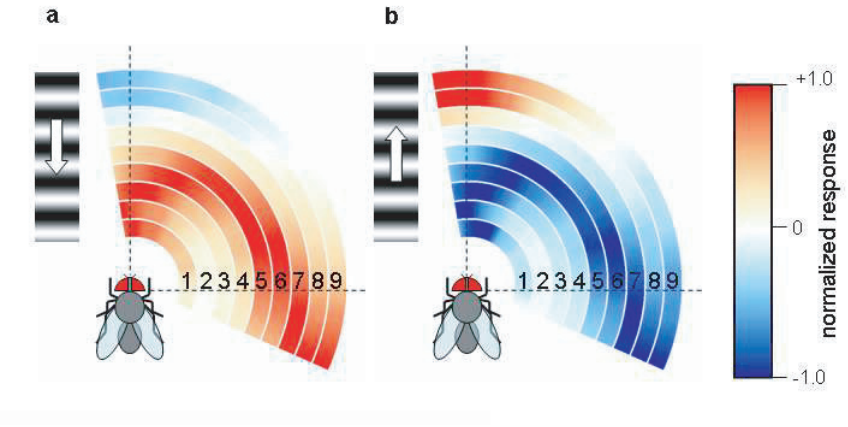

Figure 2. Sensitivity, displayed in false color code, of VS cells to vertical motion as a function of the stimulus azimuth. (a) Responses of VS cells (VS1–VS9) to downward motion, (b) responses of VS cells to upward motion. The peak response shifts with increasing azimuth from VS1 to VS9. All responses have been normalized with respect to the peak response to down- or upward motion, respectively. Reprinted with permission from [15].

It has been found that the electrical coupling of the VS cells significantly broadens their tuning for downward motion along the horizontal axis of the visual field [11]. Photo-ablations of single VS cells narrowed the tuning width of nearby cells [12], demonstrating that these neurons indeed receive information from their neighbors via electrical synapses.

A closer inspection of the receptive fields reveals that outside of the part of the visual field where a VS cell responds most strongly, it exhibits different local preferred directions [14, 16]. The global arrangement of local preferred directions resembles a rotational flow (see figure 3). This finding led to the hypothesis that VS cells encode information about rotational movements as induced by self-motion [16, 17]. In particular, it was proposed that the axis of rotation should be encoded by the VS cell responding most strongly, i.e. by the cell whose response field matches the rotational flow field best [16]. However, this hypothesis does not take into account the response behavior of the local motion detectors, especially when confronted with images representing natural scenes [10] characterized by an inhomogeneous contrast distribution.

2. Results

2.1. Input hypothesis

The response properties of the VS cells to moving gratings can be best described by assuming that they receive input from motion detectors of the correlation-type [18, 19]. For VS cells, the preferred direction of these so-called Reichardt detectors [20]–[25], schematically depicted in figure 4, is downward, the null direction is upward. This assumption neglects inputs from non-vertically tuned local motion detectors or from further tangential cells presumably responsible for the non-vertical direction preferences in the receptive fields of VS cells (see figure 3). In particular, it could be demonstrated that VS7/8 receives input from the HSN cell which is sensitive for horizontal motion in the dorsal part of the visual field [11]. However, it has been

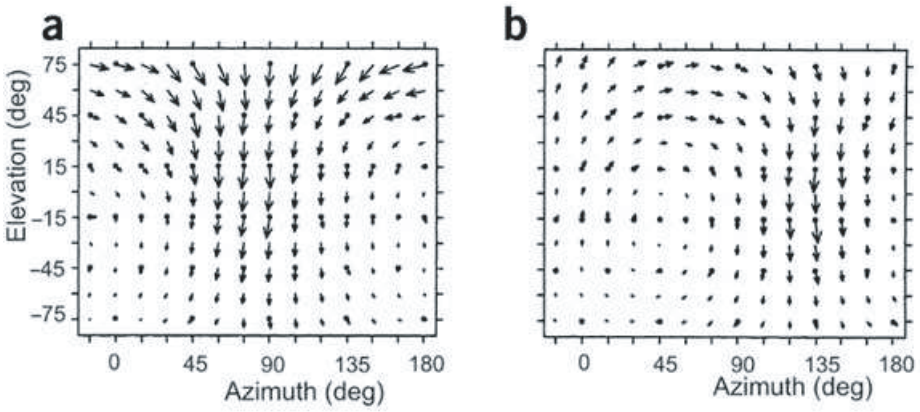

Figure 3. Response maps of a VS5 (a) and VS8 (b) cell. The orientation of the arrows indicates the preferred direction of the corresponding cell at this position; the arrow length corresponds to the response strength. The receptive fields exhibit a broad tuning for downward motion. Both neurons show a main sensitivity to downward motion at an azimuth of 90° and 135°, respectively. Adapted with permission from [14].

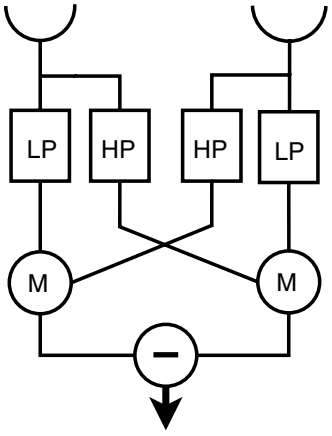

Figure 4. The Reichardt detector estimates motion by correlating the signals of adjacent image locations. It consists of two subunits. The luminance signal at each location is fed through a low-pass filter and afterwards multiplied with the high-pass filtered input from the neighboring location. The output signals of both subunits are finally subtracted. For motion in 2D a pair of Reichardt detectors is assumed at each image location, one oriented horizontally and one oriented vertically. The responses of both detectors are then interpreted as the x- and y-component of the local motion vector, respectively.

shown that homogeneous large-field downward motion can also effectively excite VS cells. Moreover, the V1 cell that integrates input from VS1 to VS3 does not respond significantly stronger to rotation than to translation [26]. Thus, omitting inputs from further tangential cells or local motion receptors providing information about horizontal motion seems to be a justifiable simplification. According to our assumptions, a rotational self-motion in the horizontal plane

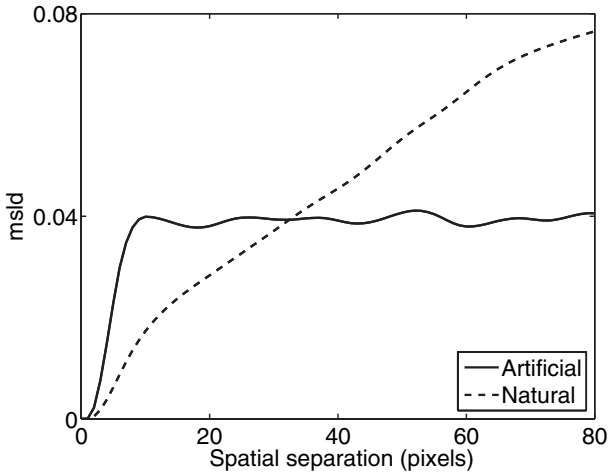

Figure 5. Contrast distribution of an artificial and a natural image (see figure 6(a) and (b)): the pixel intensities of the artificial image are normally distributed with mean and standard deviation of 1. Both images were blurred by a 3×3 box filter. For comparison, we calculated the msld between image pixels as a function of relative separation between these pixels. The natural image exhibits an msld that monotonically increases with increasing pixel separation. In contrast, the msld of the artificial image is constant for a spatial separation larger than 8 pixels. For smaller separations the msld of the artificial image decreases since it was blurred making neighboring pixels more similar.

induces no potential shift in the VS cell whose azimuth of maximum sensitivity to downward motion matches the azimuth of the center of rotation. In the remaining VS cells increasing negative or positive potential shifts are induced in dependence of the distance of their azimuth of maximum downward motion sensitivity from the axis of rotation. In contrast, a translational upward or downward motion would yield constant positive or negative potential shifts in all VS cells. However, due to its intrinsic response properties, the Reichardt detector strongly deviates from an ideal speedometer where the response depends linearly on velocity. First of all, the response strength of theses detectors decreases for velocities higher than a certain optimum velocity [27]. Second, Reichardt detectors are strongly dependent on the local luminance and contrast of the moving image [10, 28].

To study the influence of these characteristics of Reichardt detectors on the processing of moving natural images, we defined a measure quantifying the contrast distribution of images, the mean squared luminance difference (msld) between image pixels as a function of relative separation between these pixels. Typically, neighboring pixel values within natural images are highly correlated in luminance intensity [29]. Accordingly, the msld of an exemplary natural image is low for small spatial separations (see figure 5). However, it increases with increasing distance between pixels. Thus, the natural image is characterized by an inhomogeneous contrast distribution for larger spatial separations. Conversely, an artificial image with normally distributed luminance intensities shows a rather constant msld (see figure 5), i.e. the contrast is homogeneously distributed.

To investigate the impact of the contrast distribution on the response properties of the motion detectors, we used the artificial and the natural image as visual stimuli for a 2D array of Reichardt detectors (for more details see appendix A). Each image was rotated clockwise

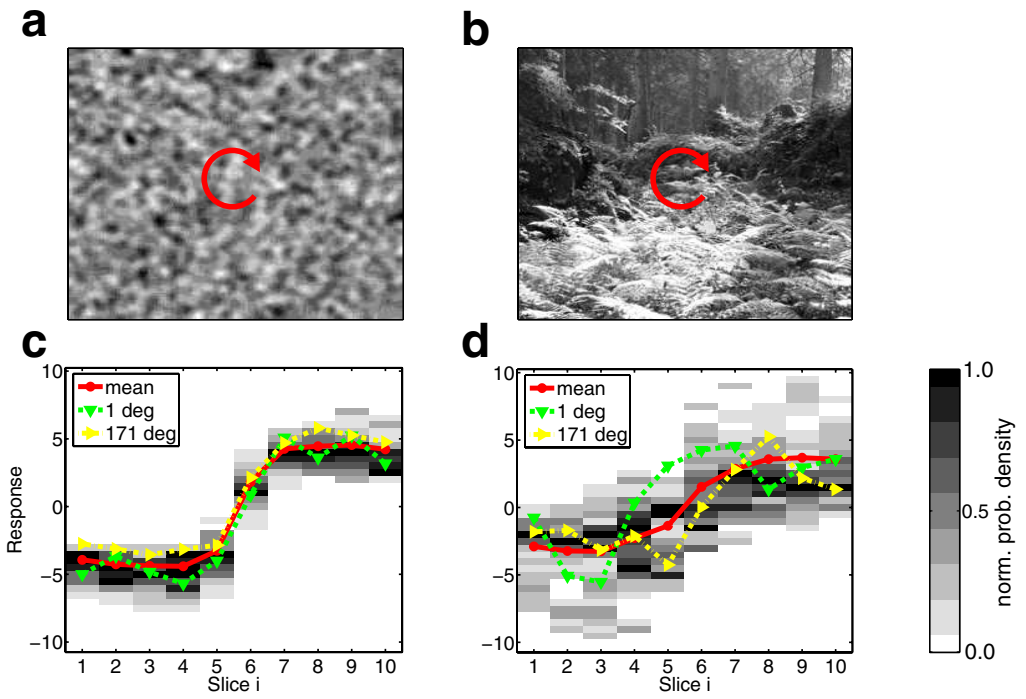

Figure 6. The responses of motion detectors of the Reichardt-type depend on the texture and contrast distribution of an image. We rotated an artificial (a) and a natural image (b) clockwise by 360° around its center (indicated by the red arrows) at a speed of 0.3° ms^{-1}, respectively. (c),(d) The central part of each image was divided into 10 adjacent slices. For each slice the integrated vertical response components of a Reichardt detector array were calculated every 3 ms. The normalized distributions of the integrated responses for each slice are displayed in grey scale code along the *y*-axis. Note that the mean variance of the integrated slice responses is significantly smaller for the artificial image compared to the natural image. Besides the mean values, two snapshots of the responses at two different rotation angles (1° and 171°) are also shown.

by 360° around its center with a velocity of 0.3° ms^{-1} (see figure 6(a) and (b)). Within ten adjacent slices, we integrated for each rotation angle the vertical response components of the corresponding local motion detectors. The slices might be interpreted as the receptive fields of isolated VS cells, which are not electrically coupled to their neighbors and, therefore, receive input exclusively from local Reichardt detectors impinging on to their dendrite. Overlapping receptive fields of adjacent VS cells were accounted for by smoothing output signals of the 2D array of Reichardt detectors (see appendix A). We calculated for each slice a histogram over the integrated local motion detector signals. The resulting distributions were normalized to their corresponding peak value and are plotted along the *y*-axis in figures 6(c) and (d).

The mean responses over 360° to the rotating image increase with the distance of the corresponding slice to the rotation center, i.e. they become stronger with increasing velocity. However, within the peripheral slices the mean response slightly decreases in both the cases indicating that, in these parts, the velocity is higher than the optimum velocity of the Reichardt

detectors. The responses to the natural image exhibit a significantly higher mean standard deviation ($\sigma = 2.06$) compared to the artificial image ($\sigma = 1.17$).

Snapshots at different times during rotation exemplify the texture and contrast dependence of the detector signals, especially in case of the natural image (see figure 6(d)). In each case the responses do not increase linearly as a function of velocity. Instead, they vary strongly around the mean response. Consequently, optic flow parameters such as the azimuth of the axis of rotation do not clearly correlate with single slice responses at each point in time. Moreover, with a membrane time constant of $\tau = 1.4$ ms [8], isolated VS cells would not be able to integrate signals over a longer time interval to approximate a more stable mean response pattern. Instead, some further processing or synaptic coupling of the VS cells seems to be necessary to robustly encode optic flow information.

2.2. Realistic model

Our work is based on a biophysically realistic model presented by [10]. In this model, the individual neurons were represented as detailed compartmental models reconstructed from image stacks obtained by two-photon microscopy. Electrical synapses were implemented as resistances located at the axonal terminals. To account for the reciprocal inhibition between VS1 and VS10, a negative conductance was used.

In our approach, we modeled the mutual inhibition between VS1 and VS10 by two inhibitory synapses: the first one inhibits VS10 in dependence of the presynaptic membrane potential at the axonal terminal of VS1 and the second one inhibits VS1 in dependence of the membrane potential of VS10. The steady-state conductance of each inhibitory synapse is described by a sigmoid function of the presynaptic potential with variable slope, center and maximum conductance (see appendix C.2). The resulting synaptic current is given by equation (C.4). Since VS cells are thought to encode information by membrane potential shifts, any active membrane mechanisms were neglected. Moreover, the membrane potential of the VS cells depends nearly linearly on currents up to 2 nA inducing a membrane potential shift of about 8 mV for an input resistance of about 4 MΩ [8]. For larger currents an increasing outward rectification occurs.

For simplicity, we summed up the synaptic inputs provided to one cell as elicited by large-field motion to one current injected at the dendritic root. VS cells respond to a global visual stimulation with potential shifts up to 10 mV [30]. In order to yield potential shifts of realistic strength, input patterns driven by Reichardt detectors in response to a large-field motion had to be scaled such that the inputs to the VS cells approximately range from -2.5 to 2.5 nA.

In order to adapt the biophysically realistic model, certain parameters such as membrane capacitance, axial resistance and the strength of the axonal gap junctions had to be determined. Therefore, these parameters had to be adjusted such that simulations carried out with NEURON [31]–[33] would produce results roughly equal to double-cell recordings published in [8] and [11]. We adjusted these parameters iteratively using genetic algorithms. The time-consuming task of evaluating a large number of parameter combinations in each iteration step was executed in parallel by scheduling the single simulation runs on an InfiniBand/Opteron computer cluster with 128 processors (http://infiniband.in.tum.de).

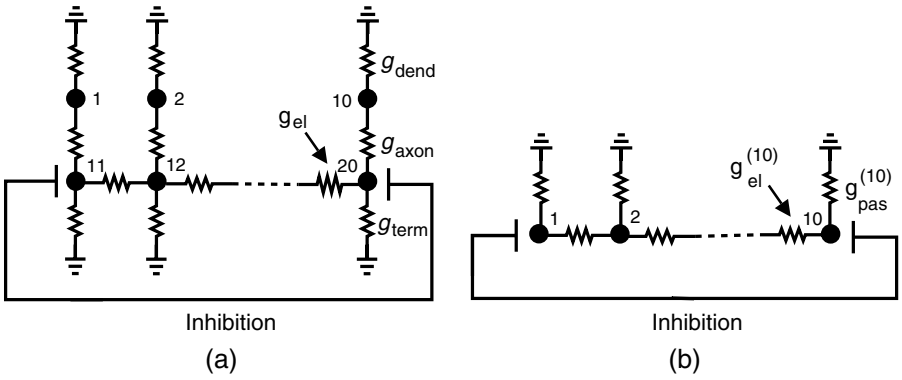

Figure 7. Simple compartment models derived from a biophysically realistic model. (a) 20 compartment model: each neuron consists of two compartments, namely a dendritic and an axonal compartment, connected by a resistance with conductance g_{axon}. Both have a passive membrane conductance g_{dend} and g_{term}, respectively. The lower (axonal) compartments of neighboring cells are connected via electrical synapses with conductance g_{el}. The mutual inhibition between VS1 and VS10 is modeled by a negative conductance with absolute value g_{inh} (see below). (b) 10 compartment model: each neuron consists of one compartment only. Neighboring cells are electrically coupled. Each cell has a passive membrane conductance g_{pas}.

2.3. Reduction to a simplified linear model

Within this study, we viewed the VS network as a system mapping a dendritic synaptic input on to membrane potentials at the axonal terminals where these neurons target postsynaptic cells. To start off with a most simple model, we linearized the realistic VS model by eliminating the inhibitory synapses and reduced it to an equivalent circuit. This allowed us to calculate the steady-state potentials at the axonal terminals when injecting current into the dendritic root where synaptic inputs are summed.

To construct such an electric circuit we derived a 20 by 20 matrix **M** from simulations, which we will refer to as resistance matrix (see also appendix C.1). We arranged the matrix **M** in the following way: columns/rows $1, \ldots, 10$ correspond to the dendritic root compartments of VS1–VS10, while columns/rows $11, \ldots, 20$ correspond to the axonal terminal compartments of VS1–VS10. The entry (i, j) of the symmetric matrix **M** corresponds to the steady-state potential of compartment i resulting from injecting current of 1 nA into compartment j. The inverse, **G**, of the resistance matrix can be interpreted as the conductance matrix corresponding to a circuit as depicted in figure 7(a) not considering the mutual inhibition. Within this circuit, individual VS cells are represented by two dimensionless compartments each: one corresponding to the dendritic root and the other to the axonal terminal of the respective neuron. The axonal compartments are coupled by electrical synapses. The conductance values used for the various resistances, g_{dend}, g_{axon}, g_{term} and g_{el}, are derived from **G** (for the definition of the conductances see figure 7). For simplicity, we calculated for each of these conductances the mean value. The parameters for the 20 compartment model are summarized in table C.1.

2.4. Eigenanalysis

2.4.1. Discrete cable. The steady-state potentials $V = [V_1, \ldots, V_{20}]^T$ given a current input $J = [J_1, \ldots, J_{20}]^T$ can be expressed by the following matrix equation:

$$V = \mathbf{M}\, J, \tag{1}$$

where the resistance matrix $\mathbf{M}$ is the inverse of the conductance matrix $\mathbf{G}$ corresponding to the 20 compartment model without inhibition. When only interested in the axonal membrane potential output given a dendritic current input, equation (1) can be reduced to

$$V = \mathbf{M_{10}}\, J, \tag{2}$$

where J is now a 10D vector. The 10 by 10 conductance matrix $\mathbf{G}_{10} = \mathbf{M}_{10}{}^{-1}$ corresponds to an equivalent electric circuit as depicted in figure 7(b) (without inhibition) and can be derived from $\mathbf{G}$ according to equation (C.1). Each neuron consists of one compartment with leak conductance $g_{\mathrm{pas}}^{(10)}$. Neighboring cells are connected via electrical synapses. The resulting 10 compartment model represents a discretized electrical cable with axial conductance $g_{\mathrm{el}}^{(10)}$ and membrane conductance $g_{\mathrm{pas}}^{(10)}$. The conductance matrix $\mathbf{G}_{10}$ reads as

$$\mathbf{G_{10}} = -\mathbf{D}\, g_{\mathrm{el}}^{(10)} + \mathbf{I}\, g_{\mathrm{pas}}^{(10)}, \tag{3}$$

with

$$\mathbf{D} = \begin{bmatrix} -1 & 1 & 0 & & 0 \\ 1 & -2 & 1 & & \\ & \ddots & \ddots & \ddots & \\ & & 1 & -2 & 1 \\ 0 & & & 1 & -1 \end{bmatrix}.$$

The conductances $g_{\mathrm{pas}}^{(10)}$ and $g_{\mathrm{el}}^{(10)}$ are related to the 20 compartment model by equations (C.2) and (C.3).

The matrix $\mathbf{G}_{10}$ has discrete cosine functions as eigenvectors. The kth element of the ith eigenvector is given by

$$S_{i,k} = \cos(\pi\ (k - 0.5)\ (i - 1)/10), \quad k = 0, \ldots, 9, \tag{4}$$

where the eigenvectors S_i, with $i = 1, \ldots, 10$, are increasingly ordered according to their frequency. The eigenvector S_i has frequency $(i - 1)/2$.

The form of the eigenvectors comes from the cable structure of the 10 compartment model when neglecting the mutual inhibition. $\mathbf{G}_{10}$ represents a conductance matrix for a discretized cable with sealed ends, i.e. $\partial V/\partial x = 0$ at both ends (von Neumann boundary condition). Note that $\mathbf{D}$ has the same eigenvectors as $\mathbf{G}_{10}$. The matrix $-\mathbf{D}[\mu S]$ represents a conductance matrix for a discretized cable without leak conductance. In this case, the current flow within the cable can be described by the 1D diffusion equation, i.e. $(\partial^2/\partial x^2)V(x) + J(x) = 0$ for steady-state. The eigenfunctions of $(\partial^2/\partial x^2)$ with a von Neumann boundary condition on the interval [0,1] are $\cos(\pi k x)$. Since $\mathbf{D}$ can also be interpreted as a discrete first-order approximation of the continuous second derivative operator (given a von Neumann boundary condition) [34], $\mathbf{D}$ and $\mathbf{G}_{10}$ exhibit discrete cosinusoidal eigenvectors.

Expressing equation (2) in terms of the eigenvalues and -vectors of $\mathbf{G}_{10}$ yields

$$V = \sum_{i=1}^{10} \lambda_i^{-1}\, c_i\, S_i, \tag{5}$$

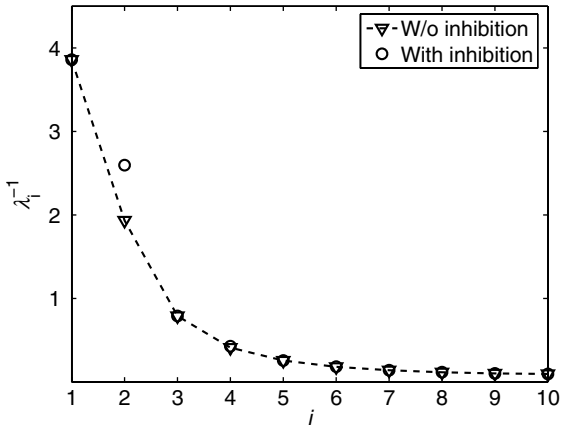

Figure 8. The input to the VS network is mainly projected on to the first two eigenvectors. The eigenvalues λ_i^{-1} of the resistance matrix $\mathbf{M}_{10}$ (see equation (5)) without inhibition (dashed line) are compared to the eigenvalues of the conductance matrix when representing the mutual inhibition by a negative conductance (see below). Due to the mutual inhibition, λ_i^{-1} is increased by about 25% for the parameters given in table C.1.

where the λ_i denote the eigenvalues of $\mathbf{G}_{10}$. The eigenvalues of $\mathbf{M}_{10}$ are λ_i^{-1} and its eigenvectors are identical to those of $\mathbf{G}_{10}$. Suppose that the matrix $\mathbf{S}$ contains the eigenvectors as column vectors. Then the coefficients $c = [c_1, \ldots, c_{10}]^T$ are given by

$$c = \mathbf{S}^{-1}\, J, \tag{6}$$

and denote the coordinates of J with respect to discrete cosine functions, i.e. multiplication by $\mathbf{S}^{-1}$ yields a discrete cosine transformation of J. In the resulting output V each coefficient c_i is weighted by the reciprocal of the corresponding eigenvalue λ_i. Thus, the eigenvalues determine which frequencies are emphasized or suppressed. Their analytical form is

$$\lambda_{k+1} = g_{\mathrm{el}}^{(10)}(2 - 2\,\cos(\pi\, k/10)) + g_{\mathrm{pas}}^{(10)}, \quad k = 0, \ldots, 9, \tag{7}$$

i.e. the eigenvalues increase with frequency. Since in equation (5) each eigenvector is multiplied by the inverse of λ_i, $\mathbf{M}_{10}$ exhibits typical spatial low-pass filter characteristics. Figure 8 shows the eigenvalues, λ_i^{-1}, of the resistance matrix $\mathbf{M}_{10}$ for the values of $g_{\mathrm{el}}^{(10)}$ and $g_{\mathrm{pas}}^{(10)}$ as derived from the realistic model. A dendritic input is mainly projected on to the first two eigenvectors.

2.4.2. Linear representation of the mutual end-to-end inhibition. So far, we deliberately neglected the reciprocal inhibition between VS1 and VS10 in the VS network. The mutual end-to-end inhibition between VS1 and VS10 is characterized by two effects: firstly, the stronger depolarized cell inhibits the other boundary cell (inhibition). Secondly, the stronger hyperpolarized cell induces a depolarization in the other cell due to suppression of transmitter release (disinhibition). Together, inhibition and disinhibition strengthen potential differences between the most medial and lateral VS cells (for a more detailed discussion see appendix C.3). As a linear approximation, this combined effect can be captured by a negative resistance. Such a resistance induces in the inhibited cell a current of inversed sign compared to the sign of the potential of the inhibiting cell.

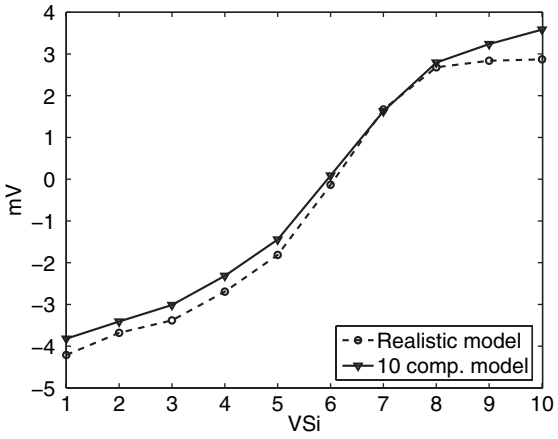

Figure 9. The VS network emphasizes the linear component of a dendritic input induced by a rotational self-motion. For illustration, we fed one of the snapshots in figure 6(a) into the realistic model and the linear 10 compartment model with inhibition. To record this snapshot, we exposed an array of Reichardt-detectors to the natural image shown in figure 6(d) rotating around its center and calculated the integrated vertical response components within 10 adjacent slices. The snapshot corresponds to the integrated slice responses at an rotation angle of 171°. For the realistic model the disinhibitory effect is smaller due to saturation of the disinhibition.

In its linearized form the mutual inhibition can be incorporated into the 20 compartment model by coupling the dendritic compartments of VS1 and VS10 via a negative conductance with absolute value g_{inh}. The corresponding conductance matrix for the 10 compartment model, $\tilde{\mathbf{G}}_{10}$, can be derived from the 20 compartment model according to equation (C.1). As illustrated by figure 9 the realistic model and the 10 compartment model (with linear mutual inhibition) show similar axonal steady-state potentials in response to a given dendritic input.

Representing the mutual inhibition by a negative conductance allows to analyze its influence on the VS network in terms of the eigenvalues and -vectors of the underlying conductance matrix. Figure 10 shows the eigenvectors of the resulting 10 compartment model weighted by the corresponding eigenvalues. In comparison to the model without inhibition, the eigenvectors are nearly unchanged, except for the second eigenvector which is nearly linearized (see figure 9).

Regarding the eigenvalues, only λ_2 is significantly changed. Increasing values of g_{inh} lower λ_2. The mutual inhibition attenuates the influence of $g_{\mathrm{el}}^{(10)}$ on the second eigenvalue in equation (7). Therefore it strengthens the contribution of the second eigenvector of $\tilde{\mathbf{M}}_{10}$ to the steady-state potential output. Multiplying S_2 with a larger factor in equation (5) emphasizes potential differences between the boundary VS cells. Hence, the stronger influence of the second eigenvector corresponds to the behavior observed for the mutual inhibition. Since the second eigenvector is linearized and the first one is constant, a dendritic input to the VS network is mainly projected on to the weighted sum of a constant and a linear vector.

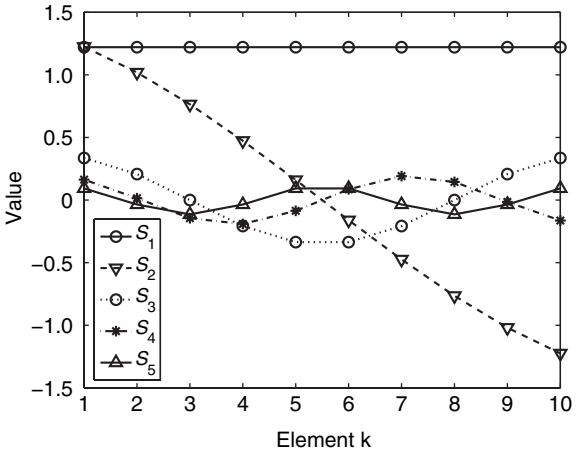

Figure 10. Weighted eigenvectors S_1–S_5 of the linear 10 compartment model with inhibition: each eigenvector is normalized to length 1 and multiplied by the inverse of the corresponding eigenvalue thus indicating their weight on the potential output. The eigenvectors are cosine-like with frequencies $f = 0, \frac{1}{2}, 1, \ldots, 2$. The first two eigenvectors represent the major components of the VS network. Note that the second eigenvector is nearly linearized due to the mutual inhibition. The model is derived from the 20 compartment model with the parameters given in table C.1.

2.5. Behavioral relevance

During free flight, flies can be directed off-course by external forces as, e.g. gusts of wind. The resulting optic flow can be described as a superposition of translatory and rotatory motion components. Our analysis of the VS network suggests that it is suited for encoding translatory up- and downward motion as well as rotation. Ideally, a vertical translation (lift) would induce a constant potential shift in all VS cells. This excitation pattern corresponds to the first eigenvector of the network. Due to the inhomogeneous contrast and texture distribution in natural scenes [35], real excitation patterns must be assumed to strongly deviate from the ideal case. However, due to the spatial low-pass filtering properties of the VS network, such an input pattern would be mainly projected on to its constant component, yielding a constant potential shift in all cells.

A rotational self-motion in the horizontal plane, as e.g. a pitch rotation, yields ideally an excitation pattern with increasing positive and negative potential shifts separated by the VS cell whose azimuth of maximum sensitivity to downward motion is located closest to the axis of rotation. Deviations from such a response vector, arising from the contrast and texture dependence of the motion detectors, are filtered out by the VS network and potential differences between the boundary cells are pronounced. In this case, the dendritic input vector is projected on to the constant and the second linearized eigenvector. A weighted sum of these two eigenvectors results in a linear vector corresponding to an input component caused by self-rotation.

Based on model simulations, the hypothesis was put forward previously [10] that the electrical coupling of the VS cells enables the network to robustly represent the center of rotation in the axonal membrane potential distribution of the whole network. As demonstrated

in the present study, an input pattern induced by a rotation is projected on to a linear vector with monotonically increasing elements. The VS cell with no (or the smallest) potential shift encodes the azimuth of the axis of rotation.

3. Conclusions

In order to study the connectivity of the VS network, we reduced a biophysically realistic model to a simplified linear model, which we subjected to an eigenanalysis. Any input to the VS network is projected on to discrete cosinusoidal functions of increasing frequency. The coefficients with respect to those discrete base functions are weighted by the inversed eigenvalues of the conductance matrix of the simplified model. Given the actual eigenvalue distribution, the VS network can be seen to reduce high dimensional inputs providing information about self-motion to its translational and rotational components. This effect is emphasized by the mutual end-to-end inhibition between VS1 and VS10.

From an information theoretical point of view, the electrical coupling of VS cells seems puzzling at first sight: the coupling makes the activity of any VS cell statistically dependent on its neighboring neuron, thus reducing the maximum entropy achievable in non-coupled neurons (for review see [36]). Moreover, the noise correlation between neighboring neurons will increase, as has in fact been demonstrated by dual recordings from visually unstimulated VS cells [11]. Such an increased noise correlation has been demonstrated to deteriorate the accuracy by which a rotation axis in the horizontal is encoded by a VS cell population [37]. On the other hand, it is intuitive to see that more positions can be encoded with overlapping receptive fields than with non-overlapping, which raises the question of the optimal coupling strength in such a network. As has been thoroughly analyzed by [38], the amount of overlap resulting in maximum information of the output population vector depends on the noise, the particular shape of the receptive field as well as the readout procedure chosen. To what extent the coupling strength as found in the VS network agrees with such a theoretical optimum remains to be determined.

Another interesting aspect is the similarity of the VS network to the analog circuits resulting from regularization methods proposed as a solution to early vision problems such as optic flow [39]. Here, an answer might be found to the question of why nature has chosen to implement the broad receptive fields by electrical coupling of neighboring VS cells instead of giving them broad dendrites in the first place. Aside from the simplicity by which such receptive fields can arise through development, another advantage might reside in the specific dynamics by which a certain output activity profile is attained in such a recurrent network compared to a straight feed-forward construction.

Acknowledgment

We are grateful to T Klug and C Trinitis for providing us access to a computer cluster.

Appendix A. Motion detection during image rotation

The pixel values of the natural image (figure 6(b)) vary between 0 and 1. As an artificial image (figure 6(a)) we created a 270×270 random image where each pixel value is normally

distributed with mean 0 and standard deviation of 1. Both images were blurred by a 3×3 box filter and rotated clockwise at $0.3^\circ\,\mathrm{ms}^{-1}$ around their center. Only a central part of 190×190 pixels was considered. During the rotation, the pixel values within this area were fed into a 189×189 array of motion detectors of the Reichardt-type (see figure 4) with downward motion as preferred direction. Each detector gets its input from two vertically neighboring pixels. During rotation the values corresponding to a certain pixel were first filtered by a low-pass filter (with a 20 ms time-constant) and multiplied with the high-pass filtered values of the downward neighboring pixel (with a time-constant of 200 ms). A second multiplication was performed in a mirror-symmetrical way, where the lower pixel values were low-pass filtered and the upper ones high-pass filtered. The output signals of both multiplications were subtracted yielding the output of the Reichardt detector. To account for overlapping receptive fields of adjacent VS cells, we smoothed the 2D array of output signals by a 2×2 box filter. We divided the Reichardt detector array into 10 adjacent slices. Within each of these the responses of all motion detectors were integrated. For each slice we calculated a histogram over the responses at each rotation angle. Each histogram comprises 42 bins ranging from -10 to 10. Its values were normalized to a maximum value of 1 and represented along the y-axis in figures 6(c) and (d).

Appendix B. Simulation

The detailed compartment models of the VS cells used for the biophysically realistic model were reconstructed from image stacks from two-photon microscopy. The realistic model was implemented using the simulation software NEURON [31, 32]. The electrical and chemical synapses are implemented as NMODL-mechanism [40] (NMODL is a model description language that allows to define neural mechanisms as e.g. synapses or active membrane conductances for NEURON). The membrane and the axial resistance are assumed to be homogeneous for each VS cell but are allowed to vary between different cells. The membrane capacitance was implicitly expressed by the membrane constant τ with $\tau = r_\mathrm{m}\, c_\mathrm{m} = 1.4\,\mathrm{ms}$ [8].

The axial and membrane resistances of each VS cell, as well as the parameters for the electrical and chemical synapses were fitted with a genetic algorithm such that steady-state potentials at the dendritic root resulting from current injections into a certain VS cell match the experimental data recorded by [11]. As a second constraint for the parameter fit the VS cells had to approximate an input resistance of about $4\,\mathrm{M\Omega}$ [8]. For the parameters as found by the genetic algorithm, the input resistances of the VS cells varied around a mean value of $3.91\,\mathrm{M\Omega}$ with a standard deviation of $0.36\,\mathrm{M\Omega}$. For illustration figure B.1 compares the experimental steady-state potentials for a $-10\,\mathrm{nA}$ injection into VS1 with the corresponding prediction by the realistic model.

Appendix C. Modeling of the VS network

C.1. Reduction of the realistic model to a simplified linear model

According to our terminology a resistance matrix refers to the inverse of a conductance matrix. Given a linear electric circuit the corresponding conductance matrix can de derived by formulating for each compartment Kirchhoff's current law. Restricting to steady-state, i.e. neglecting capacitive currents, and expressing the resulting system of equations in matrix

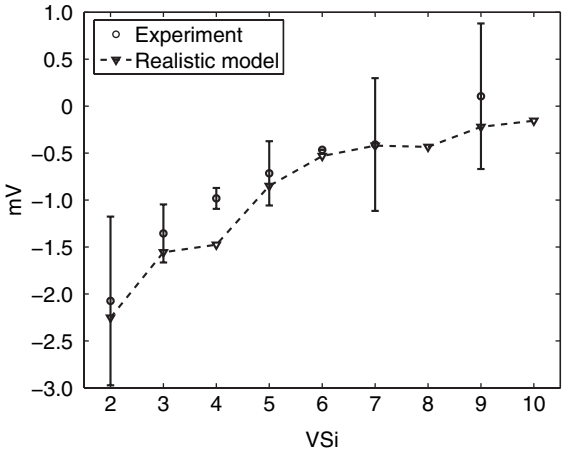

Figure B.1. The realistic model was fitted to the experimental data recorded by [11]. The experimental data for a −10 nA injection into VS1 is compared to the prediction of the realistic model.

notation yields

$$J = \mathbf{G}\, V,$$

where $J = [J_1, \ldots, J_n]^T$ denotes the currents injected into each node given the voltage vector V. The non-zero entries of $\mathbf{G}$ indicate the structure of the underlying equivalent circuit: if an entry $(\mathbf{G})_{i,j}$ is non-zero, compartment i is connected to compartment j. Inverting $\mathbf{G}$ and setting $\mathbf{M} = \mathbf{G}^{-1}$ allows to calculate the steady-state potential for a given current input to each node by

$$V = \mathbf{M}J.$$

As described above, to reduce the biophysically realistic model to a linear model, we extracted by simulations a 20 by 20 resistance matrix $\mathbf{M}$ after eliminating the chemical synapses. The conductance matrix $\mathbf{G}$, i.e. the inverse of $\mathbf{M}$, corresponds to the 20 compartment model, where each cell consists of a dendritic and an axonal compartment (see figure 7(a)). As described above, we averaged the values of the different conductances of the 20 compartment model and approximated the mutual inhibition by a resistance with negative conductance such that the whole model becomes linear and can be represented by a linear matrix equation. The conductance matrix of this model is denoted by $\tilde{\mathbf{G}}$.

If one is only interested in the axonal steady-state potentials induced by a current injection into the dendritic roots, $\tilde{\mathbf{M}} = \tilde{\mathbf{G}}^{-1}$ can be reduced to $\tilde{\mathbf{M}}_{10}$ denoting the bottom left 10 by 10 matrix of $\tilde{\mathbf{M}}$. To relate $\tilde{\mathbf{G}}_{10}$ to the conductance matrix

$$\tilde{\mathbf{G}} = \begin{bmatrix} \mathbf{A}_{1,1} & \mathbf{A}_{1,2} \\ \mathbf{A}_{2,1} & \mathbf{A}_{2,2} \end{bmatrix},$$

we formulated the following system of linear equations,

$$\begin{bmatrix} \mathbf{A}_{1,1} & \mathbf{A}_{1,2} \\ \mathbf{A}_{2,1} & \mathbf{A}_{2,2} \end{bmatrix} \begin{bmatrix} \mathbf{X}_{1,1} & \mathbf{X}_{1,2} \\ \mathbf{X}_{2,1} & \mathbf{X}_{2,2} \end{bmatrix} = \begin{bmatrix} \mathbf{I} & \mathbf{0} \\ \mathbf{0} & \mathbf{I} \end{bmatrix}.$$

Solving this system for $\mathbf{X}_{2,1}$ and setting $\tilde{\mathbf{M}}_{10} = \mathbf{X}_{\mathbf{2,1}}$ yields

$$\tilde{\mathbf{G}}_{10} = \mathbf{A}_{\mathbf{1,2}} - \mathbf{A}_{\mathbf{1,1}}\mathbf{A}_{\mathbf{2,1}}^{-\mathbf{1}}\mathbf{A}_{\mathbf{2,2}}. \tag{C.1}$$

According to equation (C.1), the conductances $g_{\mathrm{el}}^{(10)}$ and $g_{\mathrm{pas}}^{(10)}$ can be expressed in terms of the various conductances of the 20 compartment model as

$$g_{\mathrm{pas}}^{(10)} = \frac{g_{\mathrm{dend}}g_{\mathrm{axon}} + g_{\mathrm{term}}(g_{\mathrm{dend}} + g_{\mathrm{axon}})}{g_{\mathrm{axon}}}, \tag{C.2}$$

$$g_{\mathrm{el}}^{(10)} = \frac{(g_{\mathrm{dend}} + g_{\mathrm{axon}})g_{\mathrm{el}}}{g_{\mathrm{axon}}}. \tag{C.3}$$

These expressions also hold for the 20 and 10 compartment model without inhibition since they are independent of the strength of the mutual inhibition parameter g_{inh}.

C.2. Inhibitory synapses

The mutual inhibition between VS1 and VS10 is modeled by two inhibitory synapses. The steady-state conductance of each synapse in dependence of the presynaptic potential V_{pre} is described by

$$g_{\mathrm{syn}}(V_{\mathrm{pre}}) = \bar{g}_{\mathrm{syn}}/(1 + \exp(\sigma(\mu - V_{\mathrm{pre}}))). \tag{C.4}$$

V_{post} and $\bar{g}_{\mathrm{syn}}$ denote the postsynaptic potential and the maximum conductance, respectively. For the biophysically realistic model, we found best matches between the model and experiments, setting $\bar{g}_{\mathrm{syn}} = 1.5$, $\mu = 4.5$ and $\sigma = 0.6$.

The synaptic current flowing into the inhibited cell is given by

$$I_{\mathrm{syn}} = g_{\mathrm{syn}}(V_{\mathrm{pre}})\ (V_{\mathrm{post}} - E_{\mathrm{syn}}), \tag{C.5}$$

with E_{syn} as reversal potential of the synapse [41]. In our simulations, we found best results for $V_{\mathrm{m}} - E_{\mathrm{syn}} = -15\,\mathrm{mV}$.

In order to incorporate the inhibition into the 20 compartment model, we added two chemical synapses inhibiting the dendritic compartment of VS1 or VS10 in dependence of the presynaptic potential at the dendritic compartment at VS10 or VS1, respectively. The synapses are modeled in the same way and with the same parameters as for the realistic model. Simulations show that the resulting 20 compartment model and the realistic model exhibit a similar response behavior to various dendritic inputs (data not shown).

C.3. Linear representation of the mutual inhibition

The mutual end-to-end inhibition between VS1 and VS10 is characterized by inhibition of the less depolarized cell and by disinhibition of the more depolarized cell. Both features can be illustrated in a phase plane analysis. Therefore, we considered two mutually inhibiting cells whose synaptic conductance is described by a sigmoid function as given in equation (C.4), respectively. For the parameters of the synaptic conductance we used the same parameters as found for the realistic model. These two cells may be considered as VS1 and VS10 cell. Since the electrical coupling between the two cells is very small due to eight intermediate neurons, it was neglected.

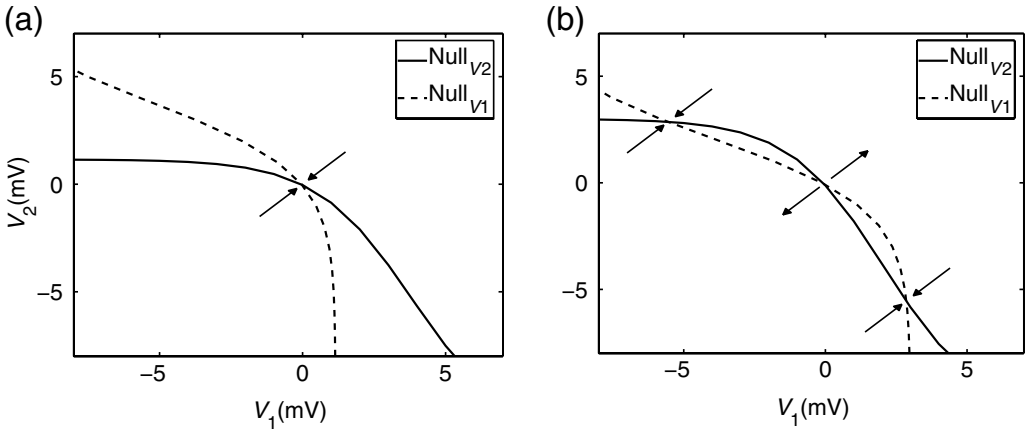

Figure C.1. Phase plane for the two network model. (a) Stable regime: the V_1 and V_2 nullclines intersect at one stable critical point, the resting potential. (b) Instable regime: besides the resting potential the V_1 and V_2 nullcline intersect at two further stable points. The resting potential is instable.

The potential time course of cell 1 and cell 2 is fully described by two nonlinear differential equations,

$$C_{\mathrm{m}}\dot{V}_1 = g_{\mathrm{syn}}(V_2)(E_{\mathrm{syn}} - V_1) + g_{\mathrm{m}}(E_{\mathrm{m}} - V_1) + J_1, \tag{C.6}$$

$$C_{\mathrm{m}}\dot{V}_2 = g_{\mathrm{syn}}(V_1)(E_{\mathrm{syn}} - V_2) + g_{\mathrm{m}}(E_{\mathrm{m}} - V_2) + J_2, \tag{C.7}$$

where C_{m} denotes the membrane capacitance. In order to study, how the system evolves in time, we considered its two nullclines in the (V_1, V_2) plane. The nullclines associated with V_1 and V_2, defined by $\dot{V}_1(V_2) = 0$ and $\dot{V}_2(V1) = 0$, read as

$$\mathrm{null}_{V1}(V_2) = \frac{g_{\mathrm{syn}}(V_2) + g_{\mathrm{m}}E_{\mathrm{m}} + J_1}{g_{\mathrm{syn}}(V_2) + g_{\mathrm{m}}}, \tag{C.8}$$

$$\mathrm{null}_{V2}(V_1) = \frac{g_{\mathrm{syn}}(V_1) + g_{\mathrm{m}}E_{\mathrm{m}} + J_2}{g_{\mathrm{syn}}(V_1) + g_{\mathrm{m}}}. \tag{C.9}$$

Figure C.1(a) shows the two nullclines at resting potential, i.e. $J_1 = J_2 = 0$. Their intersection defines the critical point where $(\dot{V}_1, \dot{V}_2) = 0$. This point is stable, i.e. after a perturbance the network will return to the same resting potential.

Any non-zero current J_1 shifts the V_1 nullcline horizontally, current injection into V_2 shifts the V_2 nullcline vertically, thus defining a new critical point. Consequently, positive current injections induce negative potential shifts in the inhibited cell (inhibition). On the other hand, since the synaptic conductance is slightly above zero at resting potential, negative current injection into one cell yields a positive potential shift in the second one due to the suppression of transmitter release (disinhibition). As a combined effect of inhibition and disinhibition potential differences between both cells are increased. This characteristic feature of the mutual inhibition is captured by a negative conductance. However, since a depolarization induced by disinhibition saturates relatively soon, the negative conductance overemphasizes this effect for a strong hyperpolarization.

The strength of the disinhibition mainly depends on the synaptic conductance and its derivative at resting potential. However, by increasing this value, the network becomes instable.

Table C.1. Values for the conductances of the 20 compartment model.

$g_{\text{dend}}[\mu S]$	$g_{\text{term}}[\mu S]$	$g_{\text{axon}}[\mu S]$	$g_{\text{el}}[\mu S]$	$g_{\text{inh}}[\mu S]$
0.18	0.03	0.11	1.0	0.06

In this case, the nullclines intersect at two additional points, whereas the critical point at (0, 0) becomes instable (see figure C.1(b)). Therefore, the network will respond to a small current injection with a jump to one of the additional critical points. Thus, the strength of mutual inhibition, represented by the parameter g_{inh}, is constrained by the stability of the network.

Modeling the mutual inhibition by a negative conductance the conductance matrix **G** for the 20 compartment model without inhibition becomes

$$\tilde{\mathbf{G}} = \mathbf{G} + \mathbf{B}. \tag{C.10}$$

The 20 by 20 matrix **B** has zero entries except

$$(\mathbf{B})_{11,11} = (\mathbf{B})_{20,20} = -g_{\text{inh}}, \qquad (\mathbf{B})_{1,10} = (\mathbf{B})_{10,1} = g_{\text{inh}}.$$

The linear representation of the mutual inhibition for the 10 compartment model can derived from $\tilde{\mathbf{G}}$ according to equation (C.1). Incorporating the mutual inhibition into the conductance matrix $\mathbf{G}_{10}$ yields

$$\tilde{\mathbf{G}}_{10} = \mathbf{G}_{10} + \mathbf{C}, \tag{C.11}$$

where the 10 by 10 matrix **C** has zero entries except

$$(\mathbf{C})_{1,1} = (\mathbf{C})_{10,10} = -\frac{(g_{\text{dend}} + g_{\text{axon}})\, g_{\text{inh}}}{g_{\text{axon}}}, \qquad (\mathbf{C})_{1,10} = (\mathbf{C})_{10,1} = \frac{(g_{\text{dend}} + g_{\text{axon}})\, g_{\text{inh}}}{g_{\text{axon}}}.$$

C.4. Parameters for the 20 compartment model

The simplified 20 compartment model is based on the connectivity as given by the inverse, **G**, of the resistance matrix **M** derived from simulations. The mean values of the various conductances (see figure 7(a)) are shown in table C.1.

The conductance matrix and the values for the conductances of the 10 compartment model can be derived from the 20 compartment model according to equation (C.1).

References

[1] Srinivasan M V and Zhang S 2004 Visual motor computations in insects *Annu. Rev. Neurosci.* **27** 679–96
[2] Frye M A and Dickinson M H 2001 Fly flight: a model for the neural control of complex behavior *Neuron* **32** 385–8
[3] Borst A and Egelhaaf M 1992 *In vivo* imaging of calcium accumulation in fly interneurons as elicited by visual motion stimulation *Proc. Natl Acad. Sci. USA* **89** 4139–43
[4] Single S and Borst A 1998 Dendritic integration and its role in computing image velocity *Science* **281** 1848–50
[5] Strausfeld N J and Bassemir U K 1985 Lobula plate and ocellar interneurons converge onto a cluster of descending neurons leading to neck and leg motor neuropil in *Calliphora erythrocephala Cell Tissue Res.* **240** 617–40

[6] Pierantoni R 1976 A look into the cock-pit of the fly. The architecture of the lobular plate *Cell Tissue Res.* **171** 101–22
[7] Hengstenberg R, Hausen K and Hengstenberg B 1982 The number and struture of giant vertical cells (versus) in the lobula plate of the blowfly *Calliphora erytrocephala J. Comput. Physiol.* **149** 163–77
[8] Borst A and Haag J 1996 The intrinsic electrophysiological characteristics of fly lobula plate tangential cells: I. Passive membrane properties *J. Comput. Neurosci.* **3** 313–36
[9] Haag J, Theunissen F and Borst A 1997 The intrinsic electrophysiological characteristics of fly lobula plate tangential cells: II. Active membrane properties *J. Comput. Neurosci.* **4** 349–69
[10] Cuntz H, Haag J, Forstner F, Segev I and Borst A 2007 Robust coding of flow-field parameters by axo-axonal gap junctions between fly visual interneurons *Proc. Natl Acad. Sci. USA* **104** 10229–33
[11] Haag J and Borst A 2004 Neural mechanism underlying complex receptive field properties of motion-sensitive interneurons *Nat. Neurosci.* **7** 628–34
[12] Farrow K, Borst A and Haag J 2005 Sharing receptive fields with your neighbors: tuning the vertical system cells to wide field motion *J. Neurosci.* **25** 3985–93
[13] Egelhaaf M and Borst A 1995 Calcium accumulation in visual interneurons of the fly: stimulus dependence and relationship to membrane potential *J. Neurophysiol.* **73** 2540–52
[14] Krapp H G, Hengstenberg B and Hengstenberg R 1998 Dendritic structure and receptive-field organization of optic flow processing interneurons in the fly *J. Neurophysiol.* **79** 1902–17
[15] Haag J, Wertz A and Borst A 2007 Integration of lobula plate output signals by DNOVS1, an identified premotor descending neuron *J. Neurosci.* **27** 1992–2000
[16] Krapp H G and Hengstenberg R 1996 Estimation of self-motion by optic flow processing in single visual interneurons *Nature* **384** 463–6
[17] Franz M O, Chahl J S and Krapp H G 2004 Insect-inspired estimation of egomotion *Neural Comput.* **16** 2245–60
[18] Borst A 2004 Modelling fly motion vision *Computational Neuroscience: A Comprehensive Approach* (London: Champman and Hall)
[19] Borst A, Reisenman C and Haag J 2003 Adaptation of response transients in fly motion vision. II: Model studies *Vision Res.* **43** 1309–22
[20] Reichardt W 1961 *Autocorrelation a Principle for the Evaluation of Sensory Information by the Central Nervous System* (London: MIT Press) pp 303–17
[21] Borst A and Egelhaff M 1990 Direction selectivity of blowfly motion-sensitive neurons is computed in a two-stage process *Proc. Natl Acad. Sci. USA* **87** 9363–7
[22] Poggio T and Reichardt W 1973 Considerations on models of movement detection *Kybernetik* **85** 439–47
[23] Reichardt W 1987 Evaluation of optical motion information by movement detectors *J. Comput. Physiol.* A **161** 674–89
[24] Borst A 2000 Models of motion detection *Nat. Neurosci.* **3** (Suppl.) 1168
[25] Borst A 2007 Correlation versus gradient type motion detectors: the pros and cons *Philos. Trans. R. Soc. Lond.* B **362** 369–74
[26] Karmeier K, Krapp H G and Egelhaaf M 2003 Robustness of the tuning of fly visual interneurons to rotatory optic flow *J. Neurophysiol.* **90** 1626–34
[27] Borst A, Egelhaaf M and Haag J 1995 Mechanisms of dendritic integration underlying gain control in fly motion-sensitive interneurons *J. Comput. Neurosci.* **2** 5–18
[28] Haag J, Denk W and Borst A 2004 Fly motion vision is based on Reichardt detectors regardless of the signal-to-noise ratio *Proc. Natl Acad. Sci. USA* **101** 16333–8
[29] Simoncelli E P and Olshausen B A 2001 Natural image statistics and neural representation *Annu. Rev. Neurosci.* **24** 1193–216
[30] Haag J, Vermeulen A and Borst A 1999 The intrinsic electrophysiological characteristics of fly lobula plate tangential cells: III. Visual response properties *J. Comput. Neurosci.* **7** 213–34
[31] Hines M L and Carnevale N T 1997 The NEURON simulation environment *Neural Comput.* **9** 1179–209

[32] Carnevale T and Hines M 2006 *The Neuron Book* (Cambridge: Cambridge University Press)
[33] Hines M L and Carnevale N T 2001 NEURON: a tool for neuroscientists *Neuroscientist* **7** 123–35
[34] Perlmutter B A and Zador A 1999 Sparse matrix methods for modeling single neurons *Biophysics of Computation* (Oxford: Oxford University Press)
[35] Olshausen B A and Field D J 1996 Emergence of simple-cell receptive field properties by learning a sparse code for natural images *Nature* **381** 607–9
[36] Dayan P and Abbott L F 2001 *Theoretical Neuroscience: Computational and Mathematical Modeling of Neural Systems* (Cambridge, MA: MIT Press)
[37] Karmeier K, Krapp H G and Egelhaaf M 2005 Population coding of self-motion: applying Bayesian analysis to a population of visual interneurons in the fly *J. Neurophysiol.* **94** 2182–94
[38] Seung H S and Sompolinsky H 1993 Simple models for reading neuronal population codes *Proc. Natl Acad. Sci. USA* **90** 10749–53
[39] Poggio T, Torre V and Koch C 1985 Computational vision and regularization theory *Nature* **317** 314–9
[40] Hines M L and Carnevale N T 2000 Expanding NEURON's repertoire of mechanisms with NMODL *Neural Comput.* **12** 995–1007
[41] Destexhe A, Mainen Z F and Sejnowski T J 1998 Kinetic models of synaptic transmission *Methods in Neuronal Modelling: From Ions to Networks* (Cambridge, MA: MIT Press)